Sādhanā (2020)45:221
https://doi.org/10.1007/s12046-020-01464-5

Pressure dependence of dryout in a heat-generating porous debris bed

ARANYAK CHAKRAVARTY[1,2,*], PRIYANKAN DATTA[1], KOUSHIK GHOSH[1] and SWARNENDU SEN[1]

[1]Department of Mechanical Engineering, Jadavpur University, Kolkata 700032, India
[2]School of Nuclear Studies and Applications, Jadavpur University, Kolkata 700032, India
e-mail: aranyakchakravarty@gmail.com

MS received 16 April 2018; revised 17 December 2018; accepted 14 February 2019

Abstract. The primary objective of this work is to numerically study the effect of system pressure on the occurrence of dryout phenomena in heap-shaped, heat-generating porous debris beds. This is achieved using a multiphase computational fluid dynamics (CFD) model that is implemented in the framework of the commercial CFD platform ANSYS FLUENT. The model is extensively validated with available experimental data on two different aspects: pressure drop in two-phase flow through porous media and prediction of dryout in typical porous debris beds. A wide range of system pressure, relevant to severe accident conditions, is considered in this analysis in order to obtain a thorough understanding of its impact on multiphase flow and dryout occurrence in porous debris beds. This analysis is performed for different subcoolings of flooding water, which gives additional knowledge on the effects of coolant subcooling on dryout occurrence. Results indicate that dryout in debris beds occurs at progressively higher power densities as the system pressure is raised. Similar effects are observed with increase in liquid subcooling as well.

Keywords. Heat-generating porous media; multiphase flow; dryout; debris coolability; ANSYS FLUENT.

1. Introduction

Hypothetical severe accidents in nuclear reactors are characterised by a lack of adequate heat removal from the heat-generating reactor core. Such inadequacy in heat removal may cause the reactor core meltdown in an extreme situation. The molten material, thus formed, relocates to lower regions due to gravitational action, during which it may come in contact with the residual coolant pool within the reactor pressure vessel (RPV). This relocation usually takes place in the form of molten jets, which disintegrate into smaller fragments on interacting with the subcooled water pool. The fragmented material quenches and ultimately settles down on the floor of the RPV as a mass of heat-generating porous debris. It is of utmost importance to ensure sufficient cooling of the heat-generating debris, failing which the debris might undergo remelting, leading to further accident progression and possible release of radioactive materials to the environment [1].

In this regard, it becomes essential to have an estimate of maximum limit up to which the heat generated can be removed from the porous debris. This limit is characterised by the occurrence of, i.e. accumulation of, water vapour within the debris bed, and results in rapid temperature rise within the heat-generating solid phase. Experimental investigations have concluded that the principal cause of dryout occurrence in heat-generating debris beds is establishment of counter-current liquid–vapour flow within the bed. Such a flow situation resists the movement of vapour out of the debris bed and leads to vapour accumulation, and subsequently dryout of the bed, when the mass flux of vapour exceeds a critical value [2].

The flow dynamics, and the associated heat and mass transfer phenomena governing dryout occurrence, has been observed to be influenced by different thermal hydraulic parameters. Two of the most pertinent parameters among these are system pressure and temperature of the flooding water. One of the earliest reported works on the impact of pressure on debris dryout is by Squarer *et al* [3]. Reed *et al* [4] studied the effect of pressure on dryout by varying the system pressure in the range of 1–170 atmospheres for various particle sizes. The dependence of dryout on system pressure was also investigated by Miyazaki *et al* [5], DEBRIS experiments [6] and STYX experiments [7]. Observations made in these investigations indicate that the dryout limit increases substantially with increase in system pressure. This trend continues up to approximately 10 bar pressure, beyond which the dryout limit has been observed

This paper is a revised and expanded version of an article presented in "First International Conference on Mechanical Engineering" held at 'Jadavpur University', Kolkata, India during January 4-6, 2018 (INCOM-2018).

*For correspondence
Published online: 31 August 2020

to decrease with further increase in system pressure [8]. In contrast with these studies on system pressure, only limited information is available in the existing literature on the impact of flooding water temperature on debris dryout although this parameter is expected to have a significant effect on the dryout phenomena.

The experimental and numerical investigations carried out on debris dryout to date have mostly focused on debris bed configurations with one-dimensional fluid flow and as such, have largely neglected the multidimensional effects associated with a realistic heap-like debris bed [9]. This article reports the results obtained from a numerical analysis on dryout occurrence considering heap-like debris beds with respect to the effects of system pressure and temperature of flooding water. The heap-like shape is approximated with a truncated conical shape of the porous debris bed [10–12]. The numerical analysis is carried out using a computational fluid dynamics (CFD) model that is capable of handling multiphase flow, heat and mass transfer in porous media as well as clear fluids. This is implemented within the framework of ANSYS FLUENT with necessary modifications with respect to modelling of the various closure relations and solid-phase energy transport equation in porous media. The modifications are incorporated in ANSYS FLUENT with the help of user-defined functions.

2. Problem description

2.1 *Physical geometry*

A truncated conical, heat-generating debris bed is assumed to be present at the bottom of a fluid-filled cylindrical cavity. This is schematically presented in figure 1. The bottom and the side walls of the cavity are considered impermeable as well as adiabatic. The top boundary of the cavity is maintained at a constant pressure such that fluid movement takes place across this boundary. However, only liquid water is allowed to flow into the cavity while both phases can exit. The debris bed is modelled as a porous region that is homogeneous and isotropic in nature. The solid particles comprising the porous matrix are assumed to be perfectly spherical, and uniform heat generation is assumed within these solid particles only. The thermophysical properties, except fluid density, are assumed to be constant in this study. Density of the fluid phases is modelled using the Boussinesq approximation. Properties of the solid phase assumed in the present study are listed in Table 1. Symmetry is assumed to exist along the z-axis, allowing axisymmetric modelling of the flow domain.

2.2 *Governing equations*

A CFD analysis of the problem detailed in section 2.1 is carried out using the commercial CFD platform ANSYS FLUENT. The Eulerian multiphase model and the porous media model of ANSYS FLUENT are utilised in the present study to take into account the effects of multiphase flow and porous debris bed, respectively [13]. The governing transport equations are summarised here for the clear fluid region and the porous debris bed considering local thermal non-equilibrium within the porous bed.

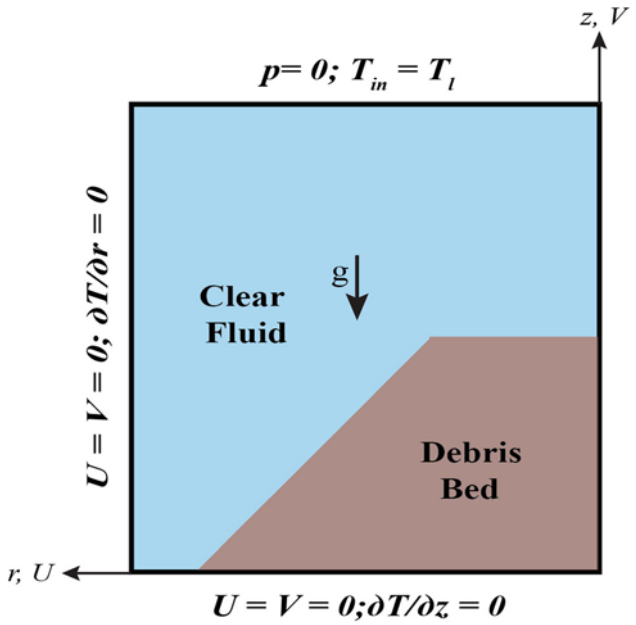

Figure 1. Schematic diagram of flow geometry and boundary conditions.

Clear fluid region

Mass transport:

$$\frac{\partial(\alpha_v\rho_v)}{\partial t}+\nabla\cdot(\alpha_v\rho_v\boldsymbol{V}_v)=\dot{m}'''_{lv}, \tag{1}$$

$$\frac{\partial(\alpha_l\rho_l)}{\partial t}+\nabla\cdot(\alpha_l\rho_l\boldsymbol{V}_l)=\dot{m}'''_{vl}, \tag{2}$$

subject to the constraint $\dot{m}'''_{lv}=-\dot{m}'''_{vl}$.

Momentum transport:

$$\begin{aligned}\frac{\partial(\alpha_v\rho_v\boldsymbol{V}_v)}{\partial t}+\nabla\cdot(\alpha_v\rho_v\boldsymbol{V}_v\boldsymbol{V}_v)&=-\nabla(\alpha_v p)\\&+\mu_v\nabla^2\boldsymbol{V}_v+\dot{m}'''_{lv}\boldsymbol{V}_{lv}\\&+R_{lv}(\boldsymbol{V}_l-\boldsymbol{V}_v)+\alpha_v\rho_v\boldsymbol{g}-\nabla\cdot(\rho_v\boldsymbol{V}'_v\boldsymbol{V}'_v),\end{aligned} \tag{3}$$

Table 1. Material properties assumed for the solid phase.

Property	Magnitude
ρ_s	4200 kg m^{-3}
λ_s	2 W/m K
$c_{p,s}$	775 J/kg K

$$\frac{\partial(\alpha_l\rho_l\boldsymbol{V}_l)}{\partial t}+\nabla\cdot(\alpha_l\rho_l\boldsymbol{V}_l\boldsymbol{V}_l)=-\nabla(\alpha_l p)+\mu_l\nabla^2\boldsymbol{V_l}+\dot{m}'''_{vl}\boldsymbol{V}_{vl}+R_{vl}(\boldsymbol{V}_v-\boldsymbol{V}_l)+\alpha_l\rho_l\boldsymbol{g}-\nabla\cdot(\rho_l\boldsymbol{V}'_l\boldsymbol{V}'_l). \tag{4}$$

Energy transport:

$$\frac{\partial(\alpha_v\rho_v h_v)}{\partial t}+\nabla\cdot(\alpha_v\rho_v\boldsymbol{V}_v h_v)=\alpha_v\lambda_v\nabla^2T_v-q'''_{vi}+\dot{m}'''_{lv}h_{vi}, \tag{5}$$

$$\frac{\partial(\alpha_l\rho_l h_l)}{\partial t}+\nabla\cdot(\alpha_l\rho_l\boldsymbol{V}_l h_l)=\alpha_l\lambda_l\nabla^2T_l-q'''_{li}+\dot{m}'''_{vl}h_{li}. \tag{6}$$

Porous debris bed

Mass transport:

$$\frac{\partial(\varepsilon_f\alpha_v\rho_v)}{\partial t}+\nabla\cdot(\alpha_v\rho_v\boldsymbol{V}_v)=\dot{m}'''_{lv}, \tag{7}$$

$$\frac{\partial(\varepsilon_f\alpha_l\rho_l)}{\partial t}+\nabla\cdot(\alpha_l\rho_l\boldsymbol{V}_l)=\dot{m}'''_{vl}, \tag{8}$$

subject to the constraint $\dot{m}'''_{lv}=-\dot{m}'''_{vl}$.

Momentum transport:

$$\frac{\partial(\alpha_v\rho_v\boldsymbol{V}_v)}{\partial t}+\nabla\cdot\frac{(\alpha_v\rho_v\boldsymbol{V}_v\boldsymbol{V}_v)}{\varepsilon_f}=-\nabla(\varepsilon_f\alpha_v p)+\mu_v\nabla^2\boldsymbol{V_v}+\frac{1}{\varepsilon_f}(\dot{m}'''_{lv}\boldsymbol{V}_{lv}+R_{lv}(\boldsymbol{V}_l-\boldsymbol{V}_v))+\varepsilon_f\alpha_v\rho_v\boldsymbol{g}+\boldsymbol{F}_{sv}, \tag{9}$$

$$\frac{\partial(\alpha_l\rho_l\boldsymbol{V}_l)}{\partial t}+\nabla\cdot\frac{(\alpha_l\rho_l\boldsymbol{V}_l\boldsymbol{V}_l)}{\varepsilon_f}=-\nabla(\varepsilon_f\alpha_l p)+\mu_l\nabla^2\boldsymbol{V_l}+\frac{1}{\varepsilon_f}(\dot{m}'''_{vl}\boldsymbol{V}_{vl}+R_{vl}(\boldsymbol{V}_v-\boldsymbol{V}_l))+\varepsilon_f\alpha_l\rho_l\boldsymbol{g}+\boldsymbol{F}_{sl}. \tag{10}$$

Energy transport:

$$\frac{\partial(\alpha_v\rho_v h_v)}{\partial t}+\nabla\cdot(\alpha_v\rho_v\boldsymbol{V}_v h_v)=\alpha_v\varepsilon_f\lambda_v\nabla^2T_v+q'''_{sv}-q'''_{vi}+\dot{m}'''_{lv}h_{vi}, \tag{11}$$

$$\frac{\partial(\alpha_l\rho_l h_l)}{\partial t}+\nabla\cdot(\alpha_l\rho_l\boldsymbol{V}_l h_l)=\alpha_v\varepsilon_f\lambda_l\nabla^2T_l+q'''_{sl}-q'''_{li}+\dot{m}'''_{vl}h_{li}, \tag{12}$$

$$\frac{\partial((1-\varepsilon_f)\rho_s c_{p,s}T_s)}{\partial t}=(1-\varepsilon_f)\lambda_s\nabla^2T_s+q'''_s-q'''_{sl}-q'''_{sv}-q'''_{si}. \tag{13}$$

Energy transport in the solid phase comprising the porous debris bed is accounted for by Eq. (13), while that in the fluid phases saturating the porous medium is taken into account in Eqs. (11) and (12). The term q'''_s in Eq. (13) represents the internal volumetric heat generation within the solid particles. Terms q'''_{sl} and q'''_{sv} represent heat transfer from the solid particles to the liquid and vapour phases, respectively, and q'''_{si} represents the contribution from boiling heat transfer. Interfacial heat transfers between liquid and vapour phases are taken into account by the terms q'''_{li} and q'''_{vi}.

2.3 *Closure relations*

Appropriate closure relations need to be considered for proper accounting of the momentum exchange terms (R_{vl}, R_{lv}, $\boldsymbol{F}_{sl}$, $\boldsymbol{F}_{sv}$) and thermal exchange terms (q'''_{vi}, q'''_{li}, q'''_{sl}, q'''_{si}, q'''_{sv}) in the momentum and energy transport equations, respectively. The closure relations utilised in the present analysis are listed in Table 2. They are not detailed in this article for conciseness. Implementation of these closure relations requires additional information regarding the

Table 2. Closure relations utilised in the analysis.

Closure term		Correlation
Momentum transfer	Interfacial drag in clear fluid region (R_{vl}, R_{lv})	Schiller and Naumann [14]
	Interfacial drag in porous debris bed (R_{vl}, R_{lv}, $\boldsymbol{F}_{sl}$, $\boldsymbol{F}_{sv}$)	Reed [15]
		Schulenberg and Muller [16]
		Rahman [17]
Heat transfer	Convection to liquid (q'''_{sl})	Ranz and Marshall [18]
	Boiling (q'''_{si})	Rhosenow [19] (nucleate boiling)
		Bromley [20] (film boiling)
	Convection to vapour (q'''_{sv})	Ranz and Marshall [18]
	Interfacial liquid–vapour heat transfer (q'''_{vi}), q'''_{li})	Ranz and Marshall [18]

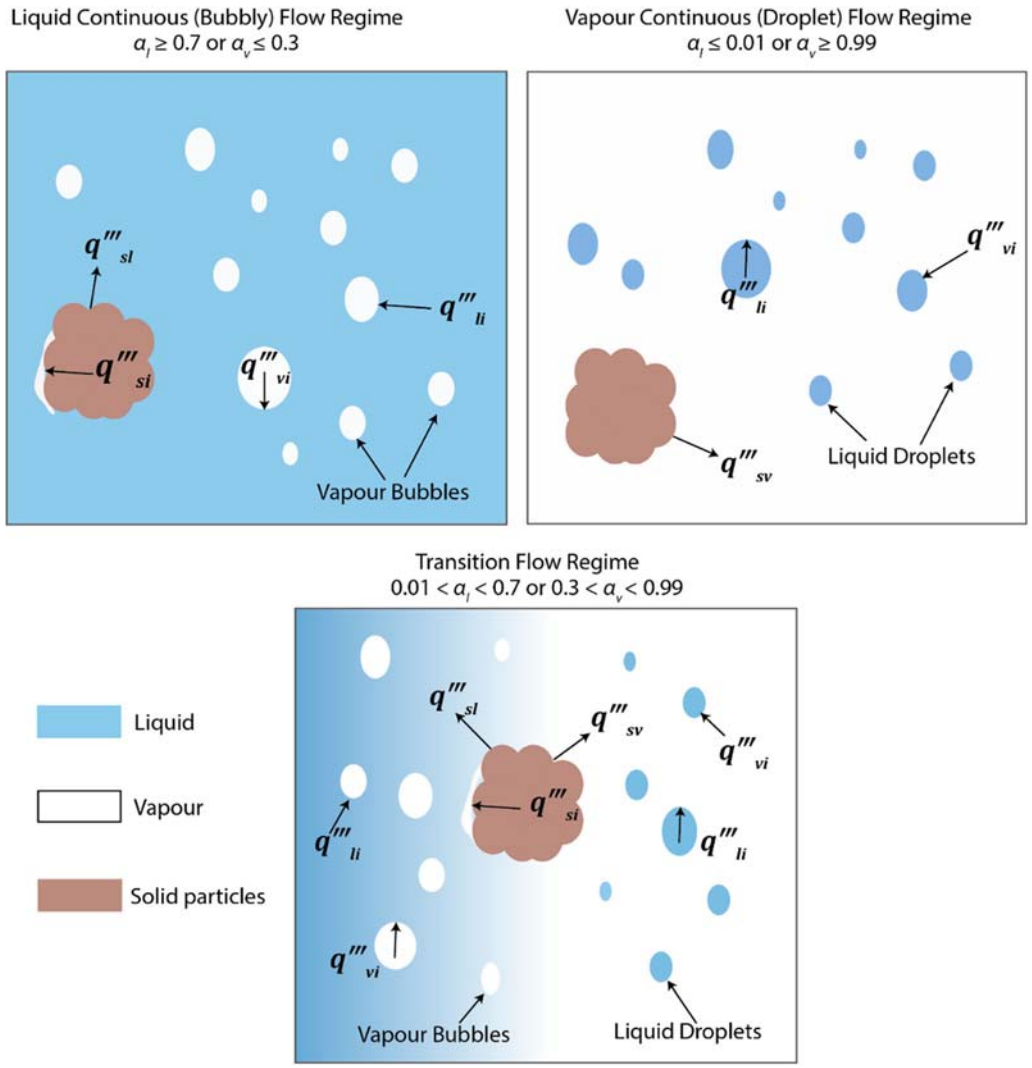

Figure 2. Heat transfer mechanisms considered among the heat-generating solid particles, liquid and vapour for different fluid flow regimes.

existing fluid flow regime. Fluid flow is considered to be demarcated into three different regimes based on volume fraction of the fluid phases. This demarcation is schematically presented in figure 2 along with the prevalent heat transfer mechanisms in each flow regime.

Liquid is considered to be the continuous phase, with vapour bubbles dispersed in it, when $\alpha_l \geq 0.7$ (or $\alpha_v \leq 0.3$). A reversed situation of liquid droplets dispersed in the continuous vapour phase is considered when $\alpha_l \leq 0.01$ (or $\alpha_v \geq 0.99$); they are referred to as the liquid continuous and vapour continuous flow regimes, respectively. Diameter of vapour bubbles (D_v) in the liquid continuous regime and of liquid droplets (D_l) in the vapour continuous regime is assumed to be 0.1 mm [21]. The interfacial exchange terms in these two flow regimes are determined with appropriate assumption of the continuous and dispersed phase parameters. A transition flow regime is considered between the liquid and vapour continuous regimes depending on the phasic volume fractions ($0.01 < \alpha_l < 0.7$ or $0.3 < \alpha_l < 0.99$). The interfacial exchange terms in the transition regime are determined as a weighted average of the terms obtained in the liquid continuous and vapour continuous regimes. The regime weighing parameter (W) is defined for the transition regime as

$$W = \frac{\alpha_l - \alpha_{l,VC}}{\alpha_{l,LC} - \alpha_{l,VC}} \tag{14}$$

where $\alpha_{l,LC}$ and $\alpha_{l,VC}$ refer to the limits of α_l for the liquid continuous and vapour continuous regimes, i.e. 0.7 and 0.01, respectively. Interfacial mass transfer between the liquid and vapour phases ($\dot{m}'''_{lv}$) is determined using the boiling heat flux (q'''_{si}) and interfacial heat fluxes (q'''_{vi}, q'''_{li}) as follows:

$$\dot{m}'''_{lv} = \frac{q'''_{si} + q'''_{vi} + q'''_{li}}{h_{v,sat} - h_{l,sat}}. \tag{15}$$

Table 3. Numerical schemes adopted for simulation.

Parameter	Scheme
Pressure–velocity coupling	Phase-coupled SIMPLE
Gradient	Least squares cell-based
Volume fraction	QUICK
Momentum, turbulent kinetic energy, turbulent dissipation rate, energy, UDS	Second-order upwind
Transient formulation	Bounded second-order implicit

Table 4. Grid-independence study in terms of minimum dryout power density.

Nominal cell size (mm)	Number of cells	Dryout power density (kW m^{-3})
5	3658	2088.772 (17.94%)
4	5771	2349.869 (7.69%)
3	9560	2545.692 (0.0%)
2	22723	2545.692

2.4 *Turbulence modelling*

Flow within the porous debris bed remains largely laminar (Re $\sim$ 1 and 10 for the vapour and liquid phases, respectively) due to large resistance offered by the solid phase against fluid flow. In the clear fluid region, however, the effects of turbulence need to be considered since Re $\sim$ 5000 and 3,00,000 for the vapour and liquid phases, respectively. A comparison of the phase velocities for the porous debris and the clear fluid region adequately highlights this aspect (see figure 8). The $k-\varepsilon$ mixture turbulence model in ANSYS FLUENT [13], with default parameters, is therefore utilised to account for the effects of turbulence in the present study.

3. Numerical procedure

The afore-described computational model is implemented in ANSYS FLUENT using the Eulerian multiphase model in conjunction with the porous media model [13]. The solid-phase energy transport equation for the porous bed is solved and the various interfacial exchange terms in the governing equations are implemented in ANSYS FLUENT with the help of various user-defined functions [22]. The numerical schemes utilised for obtaining solution of the governing equations are listed in Table 3. Table 4 summarises the findings of the grid-independence study carried out for the problem.

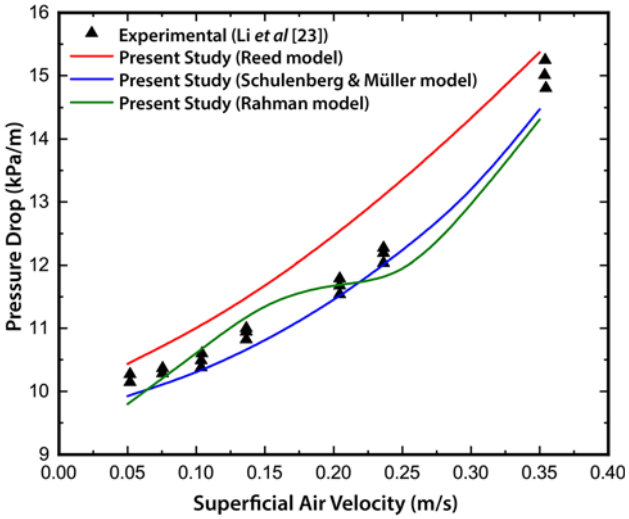

Figure 3. Comparison of pressure drop predicted by different drag models to experimental data of Li *et al* [23].

Table 5. Comparison of dryout prediction against experimental data using different interfacial drag models.

Dryout assessment method	Dryout power (kW)	Dryout power density (kW m^{-3})
Experiment [24]	39.2	2602
Present study with Reed model	40.0	2655.16 (2.04%)
Present study with Schulenberg & Muller model	39.0	2588.78 (0.508%)
Present study with Rahman model	45.0	2987.05 (14.79%)

3.1 *Validation of the model*

The implemented computational model is assessed against available experimental data for comparative purposes. Figure 3 compares the numerically predicted pressure drop to experimentally obtained data [23] for an isothermal air–water flow through a porous bed. It is evident that all the interfacial drag models can appreciably predict the experimentally obtained pressure drop in a two-phase flow situation through a porous bed.

Table 5 gives a comparison of the numerically predicted and experimentally determined dryout power density [24] for a truncated conical debris bed at an operating pressure of 1.25 bar. It can be seen that a very close prediction of the dryout power density is achieved using the Schulenberg and Muller Model. However, the model of Reed and Rahman over-predicts the dryout power density.

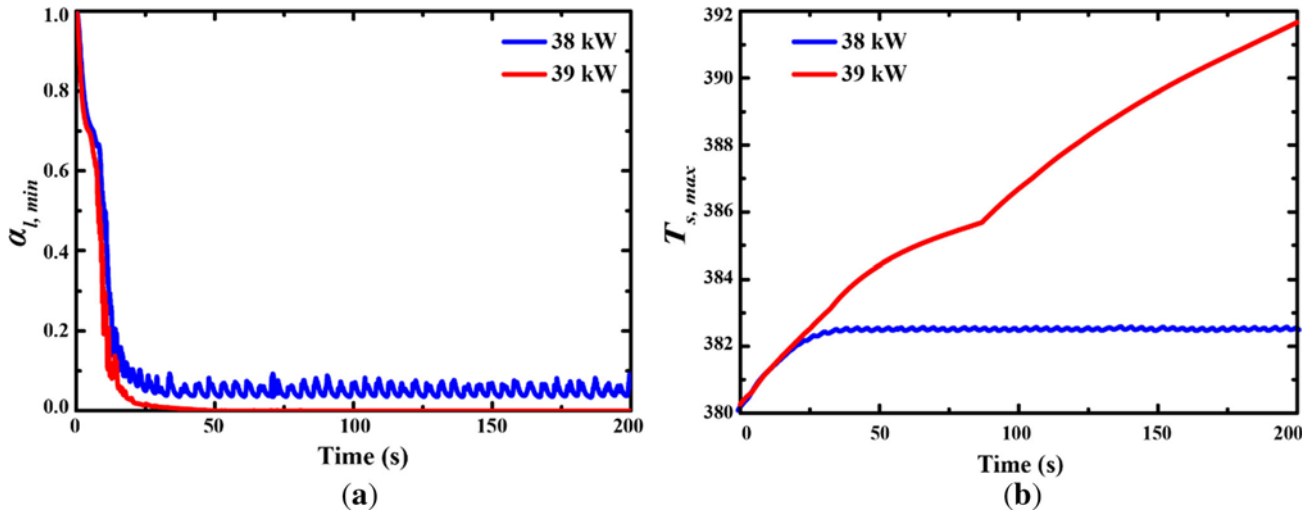

Figure 4. Temporal change of (a) $\alpha_{l,min}$ and (b)$T_{s,max}$ with Schulenberg and Muller drag model at two different heating powers.

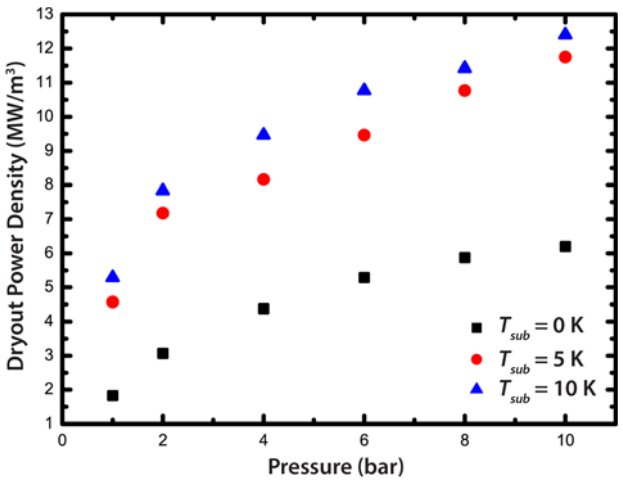

Figure 5. Variation in dryout power density with change in system pressure at three different subcooled conditions of flooding water.

3.2 *Dryout determination*

Dryout power density in Tables 4 and 5 refers to the minimum power density at which dryout is observed within the porous debris bed. This is identified by initially carrying out simulations at a low heating power and gradually increasing it in steps of 1 kW until dryout is achieved. In this respect, the following two necessary criteria are set for determining dryout occurrence numerically:

a. a region of the debris bed must become dry, i.e. devoid of liquid ($\alpha_l = 0; \alpha_v = 1$);
b. a sustained temperature rise should occur in the solid phase at that location of the bed.

They are numerically identified by determining the minimum magnitude of liquid saturation ($\alpha_{l,min}$) and the maximum magnitude of solid temperature ($T_{s,max}$) within the debris bed at each time instant. It is concluded that the bed is in a dryout state if $\alpha_{l,min}$ attains a zero magnitude and this condition is maintained for the rest of the time period, and the corresponding magnitude of $T_{s,max}$ also indicates a substantial rise (of at least 5 K) above the steady-state temperature obtained using the immediately lower power level. Although this approach identifies a dryout situation, it does not provide adequate information about the region of dryout within the bed. This is instead identified with the help of α_l and T_s distributions at different time instances.

Figure 4 shows the transient variation of $\alpha_{l,min}$ and $T_{s,max}$ at two different heating powers using the Schulenberg and Muller drag model. It can be observed that the magnitude of $\alpha_{l,min}$ decreases to a low value and fluctuates thereafter in case of 38 kW power, and the magnitude of $T_{s,max}$ fluctuates about a steady-state value near the corresponding saturation temperature ($T_{sat} = 380.259$ K). Increasing the heating power to 39 kW, however, further reduces the magnitude of $\alpha_{l,min}$ such that it becomes zero and this situation is sustained throughout the rest of the time period. The corresponding transient history of $T_{s,max}$ shows that the solid-phase temperature continues to increase with time for this heating power. Thus, it can be concluded that dryout has occurred and the minimum dryout power obtained is 39 kW.

4. Results and discussion

The impact of system pressure on the occurrence of dryout in a heat-generating porous debris bed is studied by varying the system pressure in the range of 1–10 bar, which is relevant to severe accident situations in nuclear reactors [8].

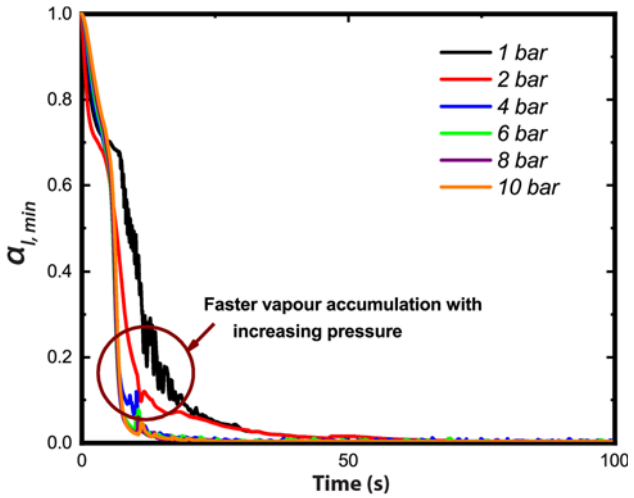

Figure 6. Temporal change in minimum liquid fraction at dryout condition for different system pressures, considering saturated liquid.

The analysis is carried out considering different subcooled states of the flooding water in order to additionally highlight the impact of water subcooling on the heat transfer dynamics and dryout occurrence.

The impact of system pressure on dryout in heat-generating porous debris is governed by the interplay of two parameters, namely vapour density and latent heat of evaporation. A higher system pressure results in a significant rise in vapour density. Vapour density increases approximately 10-fold over the pressure range considered in the present study from 0.59 kg m^{-3} at 1 bar to 5.14 kg m^{-3} at 10 bar. This effectively means that, for the same mass transfer rate, the volume occupied by the vapour phase is significantly less at higher system pressures. As such, a greater mass transfer is required from the liquid to the vapour phase for the requisite vapour accumulation necessary for dryout occurrence. The reduced vapour volume also allows a greater flow area for the liquid phase, which further enhances heat removal from the heat-

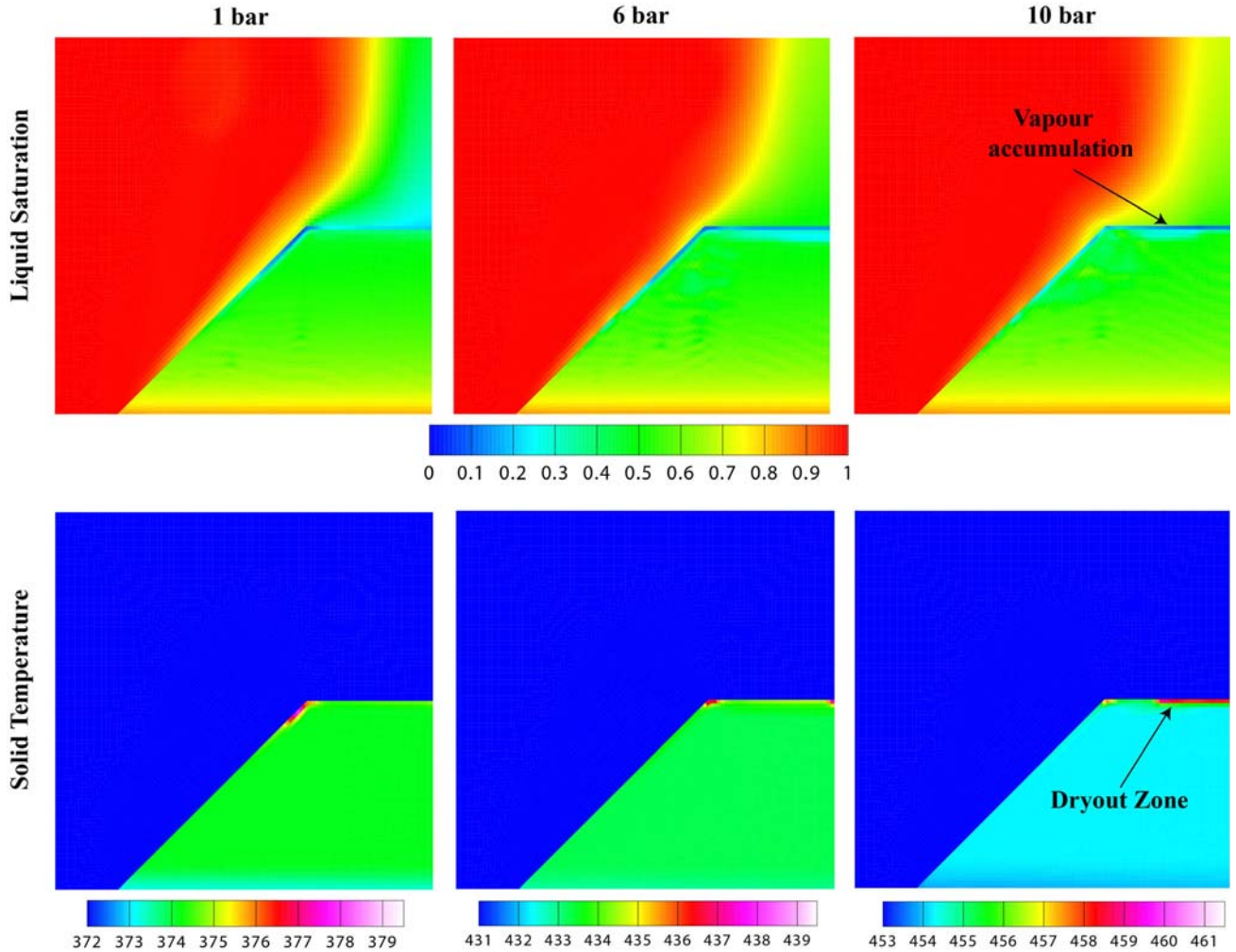

Figure 7. Liquid saturation and solid temperature distributions within the domain in a dryout situation at different system pressures, considering saturated conditions ($T_{sub} = 0$ K): 1 bar (200 s), 6 bar (200 s) and 10 bar (240 s).

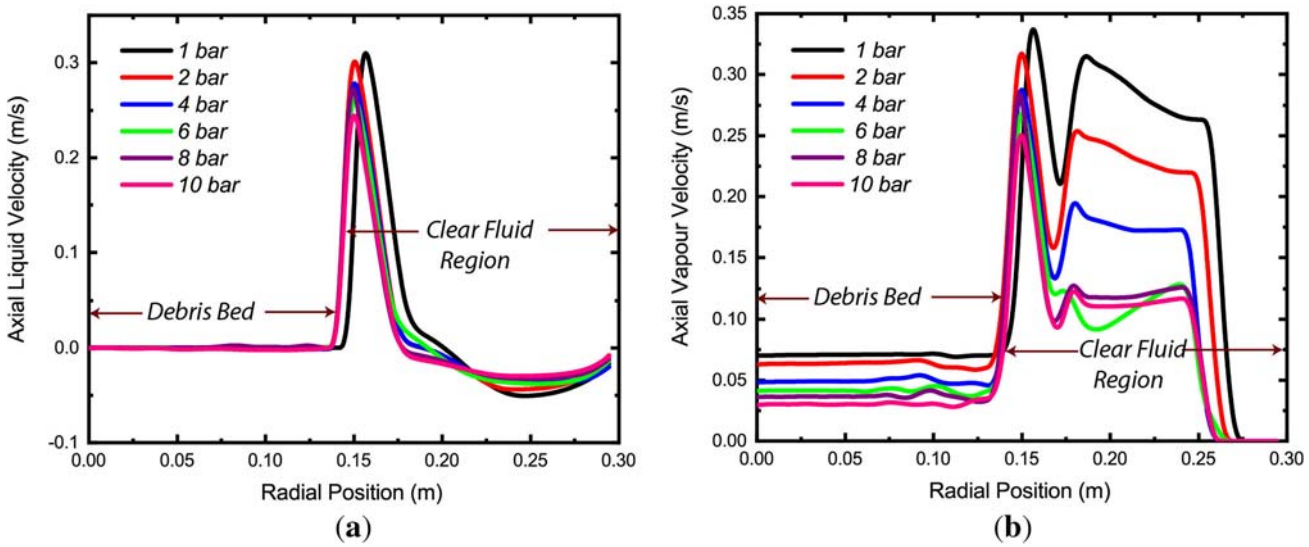

Figure 8. Axial velocity profiles of (a) liquid and (b) vapour at dryout conditions along the radial direction at $z = 0.1$ for different pressures, considering saturated liquid.

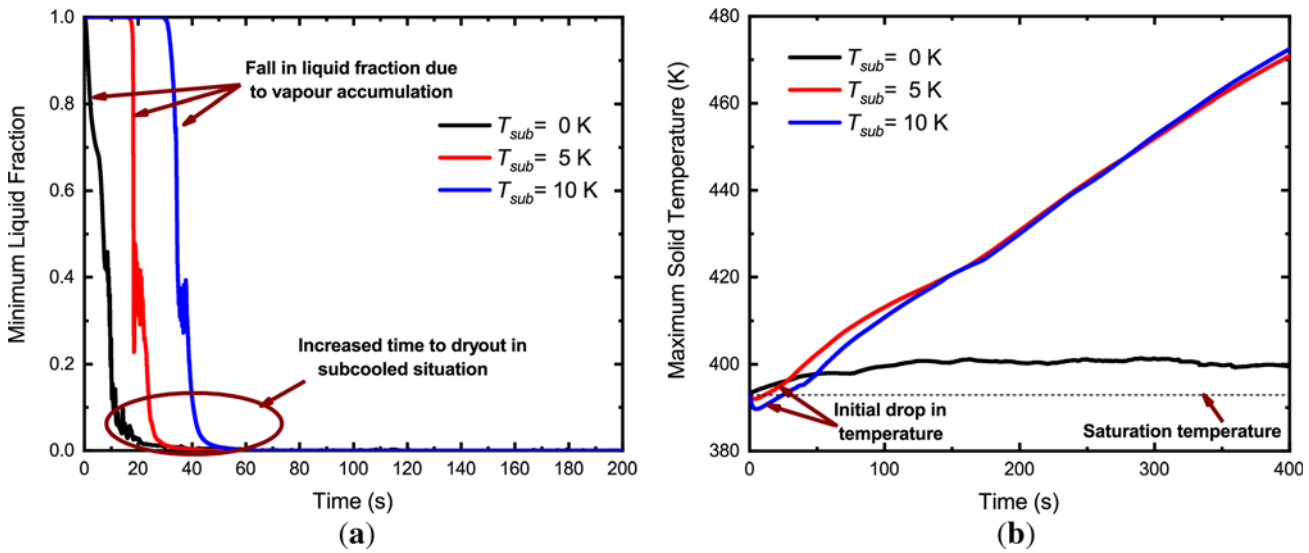

Figure 9. Temporal variation of (a) minimum liquid fraction and (b) maximum solid temperature at dryout conditions for different liquid subcoolings.

generating debris bed. An increase in vapour density, therefore, leads to a much higher requirement of heating power for dryout occurrence. In contrast, the latent heat of evaporation decreases with increase in system pressure. This results in enhanced mass transfer for a given heat generation rate (see Eq. (15)) and hence, leads to a lower power requirement for dryout occurrence. The net effect of system pressure on dryout occurrence in debris beds is, as such, determined by the combined impact of vapour density and latent heat of evaporation.

Figure 5 presents the change in minimum dryout power density with system pressure at different subcooled states of flooding water. It can be observed that dryout power density increases substantially with progressive rise in system pressure, irrespective of water subcooling. This indicates dominance of the impact of vapour density on dryout occurrence. However, as the system pressure is progressively raised, the relative increase in dryout power density reduces, indicating an increasing impact of latent heat of evaporation on dryout occurrence.

Figure 6 compares the temporal variation of minimum liquid fraction within the bed at dryout condition for different pressures, considering saturated liquid. It can be observed that a faster vapour accumulation occurs within

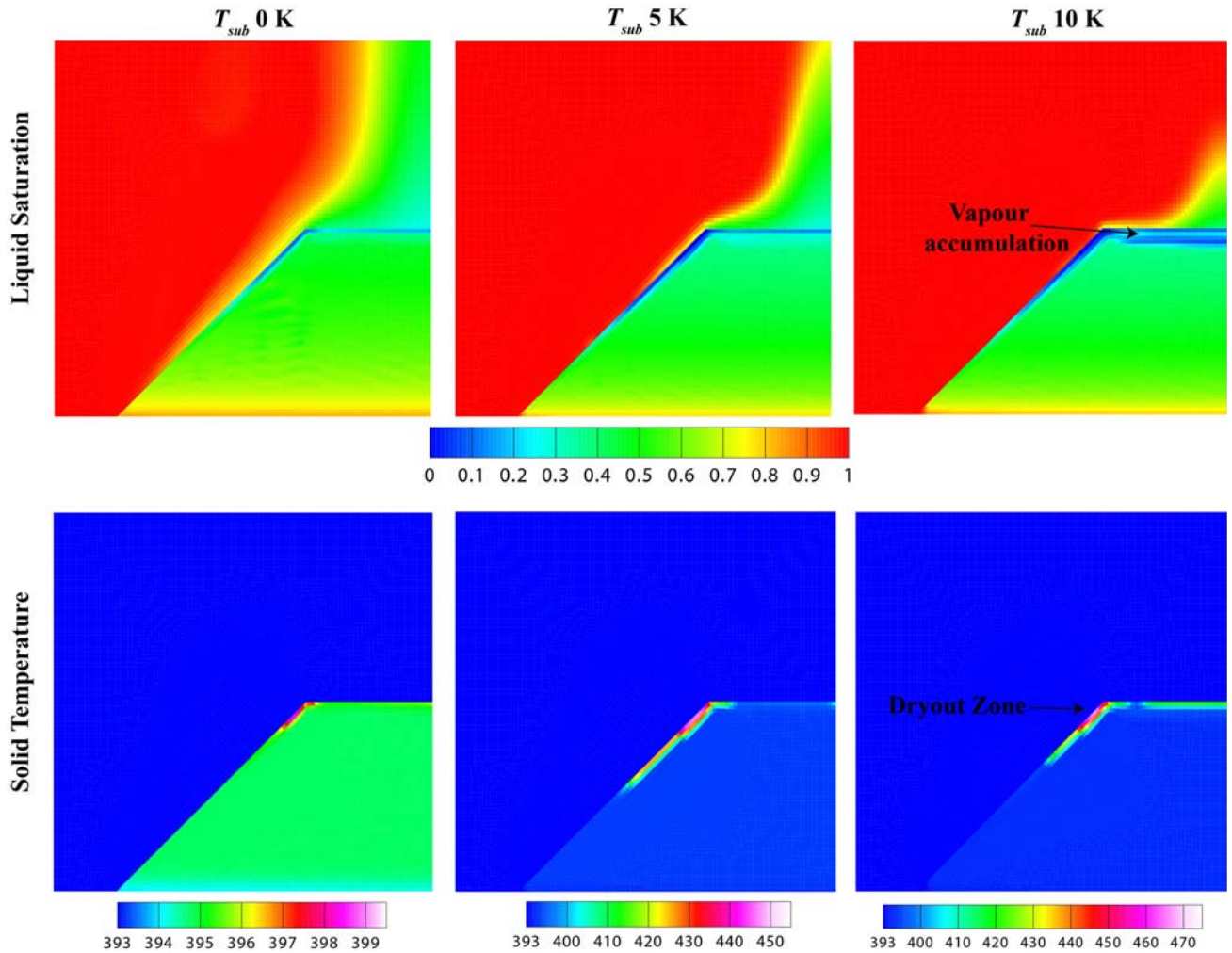

Figure 10. Axial velocity profiles of (a) liquid and (b) vapour at dryout conditions along the radial direction at $z = 0.1$ for different pressures, considering saturated liquid.

the bed as the system pressure is progressively raised due to the associated rise in dryout power density. Increase in pressure beyond 4 bar, however, does not result in any further appreciable change in the time taken for vapour accumulation. Vapour accumulation and, as such, dryout are observed to occur in the upper region of the debris bed near its interface with the clear fluid region. This is shown using liquid saturation and solid temperature distributions within the domain in figure 7. Interestingly, no major qualitative change is observed in the region where dryout occurs within the bed with change in system pressure (see figure 7). A comparison of axial velocity profiles for liquid as well as vapour phases at different system pressures (see figure 8) corroborates this observation.

It is also evident from figure 5 that if water subcooling is considered, the dryout power density increases significantly over that obtained with saturated water (i.e., no subcooling) and continues to rise with increase in subcooling. This is due to the simultaneous occurrence of boiling and condensation when subcooled water is considered. Vapour generated, due to phase change of liquid water, comes into contact with subcooled water, leading to condensation of the vapour. The required vapour accumulation for dryout, as such, becomes possible only at a very high heating power when the rate of vapour generation exceeds the condensation rate.

Figure 9 presents the transient history of minimum liquid fraction and maximum solid-phase temperature within the bed at different water subcoolings. It can be observed that a progressively greater time is required for vapour accumulation to start within the bed as subcooling is increased. This happens due to initial heat transfer from the heat-generating solid phase to the subcooled liquid phase, causing the solid-phase temperature to drop below the saturation value. Continuous heat generation, however, pushes up the solid-phase temperature beyond saturation after a certain time interval, resulting in boiling and subsequently, vapour accumulation within the bed. The regions where dryout occurs within the bed are shown in figure 10 in terms of liquid saturation and solid temperature

distributions for different water subcoolings. A marginal shift, inwards into the debris bed, is observed in location of the dryout zone as subcooling is gradually increased.

5. Conclusion

The present study uses a CFD model to numerically predict the occurrence of dryout and other associated phenomena in a heat-generating porous debris bed. The effect of system pressure on the occurrence of dryout within the porous debris bed is primarily analysed in this study. Analysis is carried out in the range of 1–10 bar, which is relevant to severe accident situations in nuclear reactors at different subcoolings of flooding water.

It is observed that the dryout power density progressively increases with rise in system pressure. Results indicate that the impact of system pressure on dryout phenomena is mainly governed by the dominance of two parameters: vapour density and latent heat of evaporation. Vapour density is observed to have a dominant effect at low system pressures while latent heat of evaporation is observed to have a greater contribution as the system pressure is raised. Subcooling of flooding water is also observed to increase the dryout power density substantially irrespective of the system pressure.

Acknowledgements

This paper is a revised and expanded version of an article titled *Pressure dependence of dryout in a heat-generating porous debris bed*, Paper No. 65, presented in the First International Conference on Mechanical Engineering held at Jadavpur University, Kolkata, India, during January 4–6, 2018. The authors are grateful to AREVA SA for providing fellowship to the first author and to Department of Science and Technology (DST), Government of India, for providing fellowship to the second author under the INSPIRE scheme.

List of symbols

c_p Specific heat capacity, J/kg K
D_l Liquid droplet diameter, m
D_p Solid particle diameter, m
D_v Vapour bubble diameter, m
$\boldsymbol{F}$ Solid–fluid drag force, kg m^{-2} s^{-2}
$\boldsymbol{g}$ Acceleration due to gravity, m/s^2
h Enthalpy, J/kg
$\dot{m}'''$ Mass transfer rate, kg s^{-1}
p Pressure, Pa
q''' Volumetric heat transfer rate, W m^{-3}
R Interfacial momentum exchange coefficient, kg m^{-3} s^{-1}
T Temperature, K
$\boldsymbol{V}$ Velocity, m/s
W Weighing function

Greek letters

α Volume fraction
ε_f Porosity
λ Thermal conductivity, W/m K
μ Viscosity, kg/m s
ρ Density, kg m^{-3}

Supercripts and subscripts

f Fluid phases
i Liquid–vapour interface
l Liquid phase
LC Liquid continuous flow regime
s Solid phase
sat Saturation value
sub Subcooling
v Vapour phase
VC Vapour continuous flow regime

References

[1] Mahapatra P S, Datta P, Chakravarty A, Ghosh K, Manna N K, Mukhopadhyay A and Sen S 2018 Molten drop to coolant heat transfer during premixing of fuel coolant interaction. In: Basu S, Agarwal A, Mukhopadhyay A and Patel C (Eds.) *Applications Paradigms of Droplet and Spray Transport: Paradigms and Applications. Energy, Environment, and Sustainability*. Singapore: Springer

[2] Schmidt W 2004 *Influence of multidimensionality and interfacial friction on the coolability of fragmented corium*. PhD Thesis, Institute of Nuclear Technology and Energy Systems (IKE), University of Stuttgart, Germany

[3] Squarer D, Pieczynski A T and Hochreiter L E 1982 Effect of debris bed pressure, particle size and distribution on degraded nuclear reactor core coolability. *Nucl. Sci. Eng.* 80(1): 2–13

[4] Reed A, Boldt K R, Gorham-Bergeron E D, Lipinski R J and Schmidt T R 1985 *DCC-1/DCC-2 degraded core coolability analysis*. Technical Report NUREG/CR-4390, SAND85-1967, Sandia National Laboratory

[5] Miyazaki K, Murai K, Ohama T, Yamaoka N and Inoue S 1986 Pressure dependence of the particle bed dryout heat flux. *Nucl. Eng. Des.* 95: 271–273

[6] Schafer P, Groll M and Kulenovic R 2006 Basic investigations on debris cooling. *Nucl. Eng. Des.* 236: 2104–2116

[7] Lindholm I, Holmstrm S, Miettinen J, Lestinen V, Hyvrinen J, Pankakoski P and Sjvall H 2006 Dryout heat flux experiments with deep heterogeneous particle bed. *Nucl. Eng. Des.* 236: 2060–2074

[8] Brger M, Buck M, Schmidt W and Widmann W 2006 Validation and application of the WABE code: investigations of constitutive laws and 2D effects on debris coolability. *Nucl. Eng. Des.* 236: 2164–2188

[9] Karbojian A, Ma W M, Kudinov P and Dinh T 2009 A scoping study of debris bed formation in the DEFOR test facility. *Nucl. Eng. Des.* 239: 1653–1659

[10] Chakravarty A, Datta P, Ghosh K, Sen S and Mukhopadhyay A 2016 Numerical analysis of a heat-generating, truncated conical porous bed in a fluid-filled enclosure. *Energy* 106: 646–661

[11] Chakravarty A, Datta P, Ghosh K, Sen S and Mukhopadhyay A 2017 Thermal non-equilibrium heat transfer and entropy generation due to natural convection in an enclosure with a truncated conical, heat-generating porous bed. *Transport Porous Med.* 116: 353–377

[12] Chakravarty A, Datta P, Ghosh K, Sen S and Mukhopadhyay A 2018 Mixed convective heat transfer in an enclosure containing a heat-generating porous bed under the influence of bottom injection. *Int. J. Heat Mass Transf.* 117: 645–657

[13] ANSYS Inc. 2012 *ANSYS FLUENT theory guide*

[14] Schiller L and Naumann Z 1935 A drag coefficient correlation. *Z. Ver. Deutsch Ing.* 77: 318–320

[15] Reed A W 1982 *The effect of channeling on the dryout of heated particulate beds immersed in a liquid pool*. PhD Thesis, Massachusetts Institute of Technology, Cambridge, USA

[16] Schulenberg T and Muller U 1987 An improved model for two-phase flow through beds of coarse particles. *Int. J. Multiphase Flow* 13: 87–97

[17] Rahman S 2013 *Coolability of corium debris under severe accident conditions in light water reactors*. PhD Thesis, Institute of Nuclear Technology and Energy Systems (IKE), University of Stuttgart, Germany

[18] Ranz W E and Marshall W M 1952 Evaporation from drops. *Chem. Eng. Prog.* 48: 141–146

[19] Rhosenow W 1952 A method of correlating heat transfer data for surface boiling of liquids. *Trans. ASME* 74: 969–976

[20] Bromley L A 1950 Heat transfer in stable film boiling. *Chem. Eng. Prog.* 46: 221–227

[21] Raverdy B, Meignen R, Piar L, Picchi S and Janin T 2017 Capabilities of MC3D to investigate the coolability of corium debris beds. *Nucl. Eng. Des.* 319: 48–60

[22] ANSYS Inc. 2012 *ANSYS FLUENT UDF guide*

[23] Li L, Kong L, Zou X and Wang H 2015 Pressure drops of single/two-phase flows through porous beds with multi-sizes spheres and sands particles. *Ann. Nucl. Energy* 85: 290–295

[24] Takasuo E 2016 An experimental study of the coolability of debris beds with geometry variations. *Ann. Nucl. Energy* 92: 251–261